# Mapping amorphous calcium phosphate transformation into crystalline mineral from the cell to the bone in zebrafish fin rays

Julia Mahamid[a], Barbara Aichmayer[b], Eyal Shimoni[c], Roy Ziblat[a], Chenghao Li[b], Stefan Siegel[b], Oskar Paris[d], Peter Fratzl[b], Steve Weiner[a], and Lia Addadi[a,1]

[a]Department of Structural Biology and [c]Department of Chemical Research Support, Weizmann Institute of Science, 76100 Rehovot, Israel; [b]Department of Biomaterials, Max Planck Institute of Colloids and Interfaces, 14424 Potsdam, Germany; and [d]Institute of Physics, University of Leoben, 8700 Leoben, Austria

Edited by David A. Tirrell, California Institute of Technology, Pasadena, CA, and approved March 3, 2010 (received for review December 10, 2009)

**The continuously forming fin bony rays of zebrafish represent a simple bone model system in which mineralization is temporally and spatially resolved. The mineralized collagen fibrils of the fin bones are identical in structure to those found in all known bone materials. We study the continuous mineralization process within the tissue by using synchrotron microbeam x-ray diffraction and small-angle scattering, combined with cryo-scanning electron microscopy. The former provides information on the mineral phase and the mineral particles size and shape, whereas the latter allows high-resolution imaging of native hydrated tissues. The integration of the two techniques demonstrates that new mineral is delivered and deposited as packages of amorphous calcium phosphate nanospheres, which transform into platelets of crystalline apatite within the collagen matrix.**

biomineralization | carbonated hydroxyapatite | cryo-SEM | microbeam x-ray diffraction | small-angle x-ray scattering

Bone mineral formation has been extensively investigated both at the cellular level and at the level of the mineral and the macromolecules. Key questions, as yet unanswered, are how mineral is delivered to the crystallization site and whether this first-formed mineral is the same as in mature bone. The possibility that calcium phosphate precursor phases are delivered and first deposited in bone has been debated for decades (1–3). In vitro precipitation of calcium phosphates from solution often progresses through the deposition of amorphous calcium phosphate (ACP) as the first-formed mineral phase (4). ACP transforms into octacalcium phosphate (OCP), which then undergoes hydrolysis to form carbonated hydroxyapatite (HAP), the mineral phase of mature bone (4). Crane et al. (5) used Raman microspectroscopy to show that in the forming cranial suture of a mouse, an OCP-like phase was deposited prior to the formation of the mature mineral. Mahamid et al. (6) showed that in the continuously forming fin rays of a zebrafish, the newly formed bone contains large amounts of ACP. Beniash et al. (7) reported the presence of ACP in the forming enamel of mouse incisors. Interestingly, recent experiments successfully reproducing oriented intrafibrillar collagen mineralization in vitro utilized anionic polypeptides (polyaspartate) for transient stabilization of amorphous mineral as a precursor for the mature HAP crystallites (3, 8). All the above studies are consistent with ACP being a precursor phase in bone formation, but direct observation of the process in situ is still absent.

The transient precursor phase strategy has been adopted by many invertebrate mineralizing groups (reviewed in ref. 9). Many of these taxa first deposit amorphous calcium carbonate, which subsequently transforms into crystalline calcite or aragonite. Because of the transient and unstable nature of the precursor phase, as well as the fact that it is often present together with the crystalline mature phase, several different techniques are needed to identify these precursor phases. These techniques also need to spatially resolve the mineral phases at different stages of formation. Microbeam x-ray diffraction and small-angle scattering provide mineralogical, particle size, and shape information at a spatial resolution in the micrometer range (10). Cryo-SEM of rapidly frozen specimens provides high-resolution images of intact tissue, not damaged by drying, but lacks information on the mineral phase. The combination of these two techniques leads to a more complete understanding of the stages of mineral formation in a biological tissue.

The tissue investigated here is the fin bony rays of the Tuebingen long fin (TL) zebrafish (*Danio rerio*) (Fig. 1). Bones from this skeletal tissue are composed of layers of plate-shaped crystals that span the collagen fibrils, the hallmark of the bone family of mineralized tissues (6). It has been previously shown that fish bones from various sources (11–15) are similar in structure and composition to mammalian bones. The advantage of studying the fin ray's continuously mineralizing tissue is that, at any given time, growth zones are present both at the extremity where elongation occurs and on the surfaces where thickening occurs as the segments mature (Fig. 1*C* and Fig. S1) (16–19). Thus both transverse and longitudinal sections through the forming end of the ray almost always include spatially resolved regions of mineralizing bone.

We present a synchrotron study of the fin bones within the native mineralizing tissue, by using spatially resolved microbeam small-angle x-ray scattering (SAXS) and wide-angle x-ray diffraction (WAXD) combined with x-ray fluorescence (XRF) imaging. We use cryo-SEM to visualize the frozen-hydrated native mineralizing tissue. The combination of these techniques, according to location, enables us to map the distribution and characteristics of the mineral phases present at the different stages of bone mineralization from the cellular tissue to the bulk mineralized bone.

## Results

**Microbeam X-Ray Diffraction and Small-Angle Scattering.** We analyzed datasets from four samples that were dissected within an hour prior to being mounted in the beam. The detailed results presented here for one specimen are consistent with the results obtained from the other specimens. Fig. 2*A* shows the investigated sample, photographed by using the beamline microscope. A detailed study was carried out on a forming tip of an individual bony ray (approximate area delineated in Fig. 2*A*: 200 μm long).

Author contributions: J.M., B.A., O.P., P.F., S.W., and L.A. designed research; J.M., B.A., E.S., C.L., S.S., O.P., and L.A. performed research; E.S. and R.Z. contributed new reagents/analytic tools; J.M., B.A., O.P., P.F., S.W., and L.A. analyzed data; and J.M., B.A., P.F., S.W., and L.A. wrote the paper.

The authors declare no conflict of interest.

This article is a PNAS Direct Submission.

[1]To whom correspondence should be addressed. E-mail: Lia.Addadi@weizmann.ac.il.

This article contains supporting information online at www.pnas.org/cgi/content/full/0914218107/DCSupplemental.

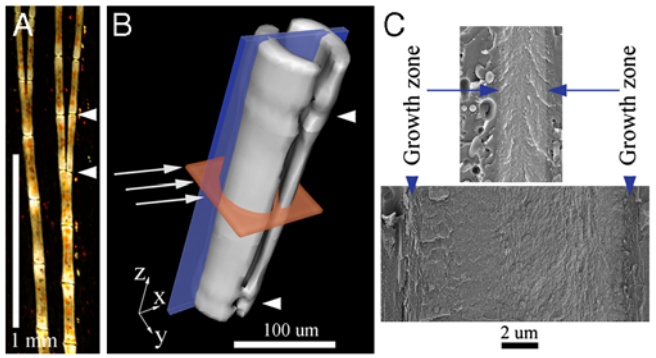


**Fig. 1.** (*A*) Representative polarized light micrograph showing two bony rays, bifurcating distally, photographed within the caudal fin tissue of a TL zebrafish. (*B*) A fin bony ray segment reconstructed from x-ray microcomputed tomography, showing the geometry of the measurements performed. Each ray is composed of many segments (one segment is shown between the two white arrowheads in *A* and *B*, ~300 μm long) and each segment is composed of two hemirays (*B*) held together by soft tissue. Continuous ray growth occurs by addition of new segments to the distal end (top in *A*, *z* direction in *B*) and thickening of each segment (*x* and *y* directions in *B*). In *B*, white arrows indicate the x-ray beam (diameter 10 μm) direction in the microbeam measurements. Two planes are marked in red and blue that represent two orientations in which the samples were observed in cryo-SEM (red: transverse sections; blue: longitudinal fracture surfaces). (*C*) Cryo-SEM micrographs of longitudinal fracture surfaces (blue plane in *B*) through native, high pressure frozen mature bone (*Bottom*) and younger bone (*Top*), represented on the same scale. The difference in bone thickness reflects the continuous thickening of the segments. Growth zones at the bone edges are indicated.

We used XRF to map the distribution of calcium in this region (Fig. 2*B*), which indicates the location of the bone within the tissue. The bone tip is calcified, with the highest concentrations of calcium found in the core toward the proximal part. A line scan across this core (Fig. 1*B* arrows, marked by color-coded rectangles in Fig. 2*B* and shown in Fig. 3*A*) shows that calcium is absent

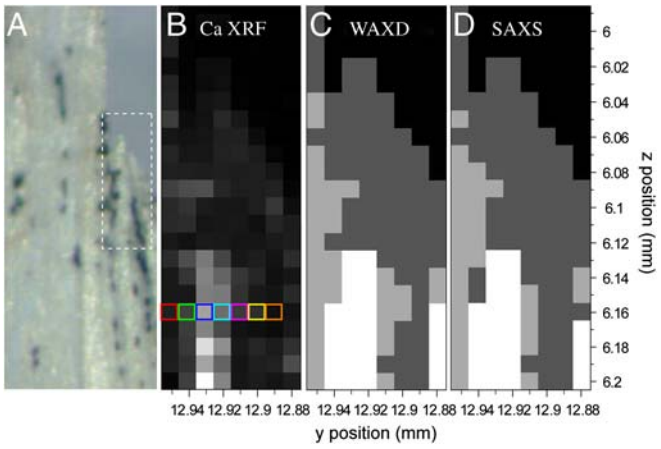


**Fig. 2.** Calcium XRF, WAXD, and SAXS simultaneously acquired with a 10-μm beam on representative TL zebrafish caudal fin bony rays within the tissue. (*A*) Light micrograph of caudal fin—delineated area (200 μm long) represents bony ray segments investigated in *B*–*D*. (*B*–*D*) Maps at 10-μm resolution of Ca XRF, WAXD, and SAXS, respectively. (*B*) Gray level indicates calcium levels (white: highest counts). Colored rectangles indicate positions across the bone for which Ca XRF, WAXD, and SAXS analysis are detailed in Fig. 3. (*C*) Mineral phases: white—bone apatite diffraction; light gray—mineral phase producing amorphous scatter; dark gray—organic tissue scattering; black—no signal. The mineral phase assignment is derived from the spectra in Fig. 3. (*D*) Particle morphologies: white—typical bone platelet scattering; light gray—spherical particles producing oscillatory scatter; dark gray—organic tissue scattering; black—no signal. The particle morphologies are derived from the spectra in Fig. 3.

on the outer side of the tip (location VII in Fig. 3*A*). We can thus expect that growth zones are located between the nonmineralized tissue and the bone core (16, 17).

WAXD data collected along the same line scan and corresponding to the Ca XRF in Fig. 3*A* are reported in Fig. 3*B*: Comparatively sharp reflections, superimposed on two large and broad peaks originating from the organic tissue, are clearly discernible in locations II, III, and IV, which correspond to the center of the bone. After subtraction of the organic tissue contributions (see *Materials and Methods*) (Fig. 3*C II*, *III*, and *IV*), these reflections can be fitted to three peaks corresponding to crystalline diffraction peaks of HAP (Fig. S2).

Both bone edges are dominated by a phase represented by a broad peak at approximately 19.4 $nm^{-1}$ ($d$ spacing = 3.23 Å) (Fig. 3*C I*, *V*, and *VI*). This broad peak indicates the presence of a highly disordered phase, with a short-range order that is apparently different from that of synthetic ACP ($d$ = 2.98 Å, Fig. S2). In some positions of the specimens, typically at the interface between HAP and the amorphous phase, the diffuse scattering is resolved into a much sharper peak with the same $d$ spacing (prominent in Fig. 3*CII*). This crystalline phase does not clearly fit any of the calcium phosphate minerals commonly associated with bone, such as OCP or dicalcium phosphate dihydrate: The peak position is close to that of one of the known OCP peaks [(501), $d$ = 3.27 Å], but the main reflection of OCP [(100), $d$ = 18.17 Å] is missing. It is noteworthy that one sample that was deliberately not completely dehydrated before the measurement did not produce any amorphous peaks but did produce pronounced diffraction peaks of the new phase at the bone edges. We therefore suspect that this unidentified crystalline diffraction could be an artifact, attributed to crystallization of the amorphous phase during specimen preparation.

Because of the electron density difference between mineral and collagen, SAXS measurements provide information on the bone mineral particles and their arrangement within the collagen fibrils on scales of 0.5–50 nm (reviewed in ref. 10). The shape of the SAXS curve varies as a function of the mineral particle shape and of the local arrangement of particles (20). SAXS data from the same 2D patterns as the WAXD data described in Fig. 3 *B* and *C* are shown in Fig. 3 *D* and *E*. Tissue background was not subtracted, because the thickness and thus the contributions of organic tissue to the scattering could not be quantified for the small-angle region. Qualitatively, the highest intensity readings (Fig. 3*D II*, *III*, and *IV*, which also have the highest calcium levels) from the center of the bone produce typical bone SAXS profiles for thin elongated HAP platelets (21). When plotted on a double-logarithmic scale, they are characterized by a slope of −4 for $q$ = 2.3–3 $nm^{-1}$. Their $c$ axes, which correspond to the largest dimension of the elongated platelets, are overall aligned with the long axis of the ray (anisotropic 2D SAXS/WAXD pattern in Fig. S3). Mineral platelet thickness was evaluated for several curves following Fratzl et al. (21). The values obtained (2.2–2.5 nm) are in agreement with typical values reported for fish and other bones (11, 21, 22). Measurements taken from both bone edges [Fig. 3 *D* and *E*: red and magenta (*I* and *V*)] give a distinct oscillatory scattering pattern, which is best seen when the data are plotted on a Kratky plot (intensity multiplied by $q^2$) (Fig. 3*E*). This pattern is strikingly different from typical bone SAXS patterns and tissue scattering (see also Fig. S4). The latter consistently produce a broad hump between 0.5 and 1 $nm^{-1}$, whereas the scattering profiles from the bone edges typically show a minimum in the same $q$ region. The oscillatory scattering pattern is reminiscent of scattering from monodisperse spheres (23). A calculated scattering function for spheres of 6 nm radius (Fig. 3*E*, *Black Curve*) shows a good qualitative agreement with the mineral scattering from the bone edges. Deviations from this model (i.e., differences in the ratio of the height of the maxima)

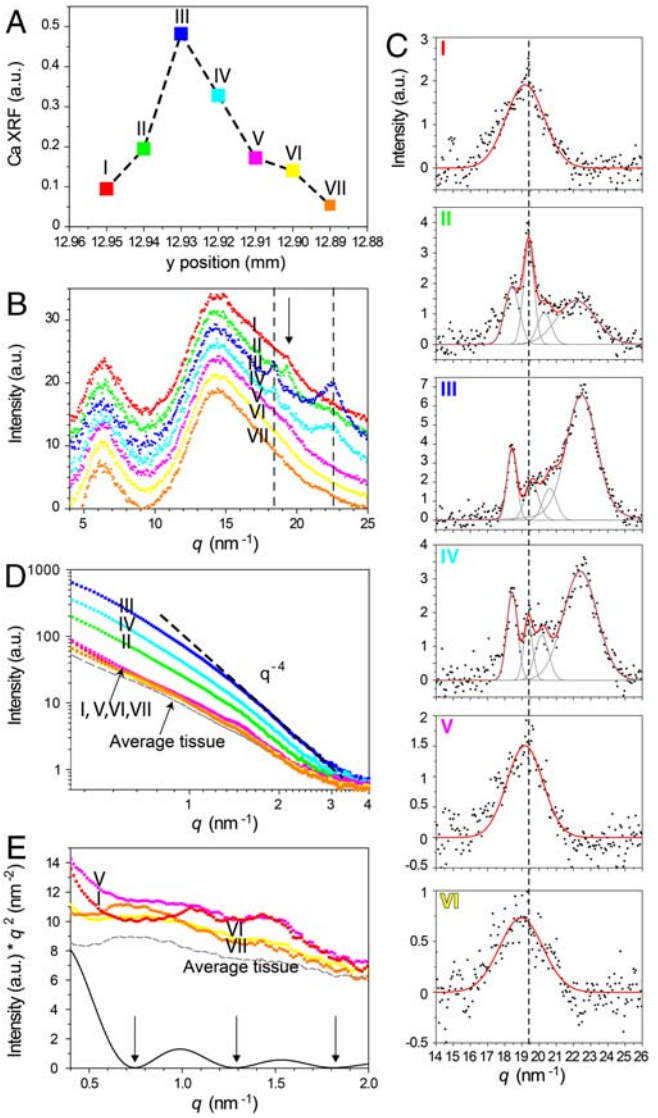


**Fig. 3.** Calcium XRF (*A*), WAXD (*B* and *C*), and SAXS (*D* and *E*) profiles of a representative line scan transverse to the fin bone long axis, indicated by rectangles in Fig. 2*B*. (*A*) Calcium levels highlight the bone profile: Highest reading (blue, III)—center of the bone; red (I), magenta (V), and yellow (VI)—bone edges/growth zones; orange (VII)—organic tissue outside the bone. The same color code and numbering are used to indicate measurement position across the bone throughout the figure. (*B*) The WAXD patterns are dominated by two very broad peaks originating from the organic tissue. Curves were normalized to the curve representing the tissue scattering at $q = 9$–$14$ nm$^{-1}$, and the intensity was shifted arbitrarily for simplified visualization; dashed black lines—carbonated hydroxyapatite reflections in the green-cyan (II–IV) curves; arrow—broad peak in the red and magenta (I, V) curves. (*C*) Data plotted in *B* (I–VI) after tissue background subtraction and peak fitting; gray lines—individual fitted peaks; red lines—overall fit. In III and IV, crystalline carbonated hydroxyapatite diffraction peaks appear at 18.4 nm$^{-1}$ (002), 20.5 nm$^{-1}$ [unresolved (102) and (210) reflections], and 22.5 nm$^{-1}$ [unresolved (211), (112), and (300) reflections]. In I, V, and VI, a disordered phase appears at 19.4 nm$^{-1}$ (*Dashed Line*), which becomes crystalline (*Sharp Peak*) in II and IV. (*D*) SAXS profiles plotted on a double-logarithmic scale. Green-cyan (II–IV) produce typical bone SAXS following Porod's approximation (slope $q^{-4}$). Measurements from bone edges and within the organic tissue produce different, low intensity scatter, better resolved in *E*. The dashed gray line is an average of 4 measurements from organic tissue at different locations, arbitrarily shifted in intensity. (*E*) Data multiplied by $q^2$ and plotted on a linear scale (Kratky plot). Red (I) and magenta (V) show two distinct minima (0.75 and 1.29 nm$^{-1}$) that coincide with minima produced in the calculated SAXS for monodisperse spheres of radius 6 nm (*Black Curve, Arrows*). Organic tissue gives a maximum at 0.7 nm$^{-1}$; the yellow (VI) curve has much scattering contribution from the organic tissue.

may arise from scattering contributions from the tissue and the mature mineral particles.

Fig. 2 *C* and *D* are 2D maps of the WAXD and SAXS results in the area of interest defined in Fig. 2*A*. Different types of scattering patterns were distinguished according to the descriptions given in the preceding paragraphs. The gray-scale coding of the maps reflects mineral and organic tissue scattering as specified in the legend (Fig. 2). The two maps are remarkably similar. We thus conclude that the newly formed mineral at the growth zones (light gray) surrounding the crystalline core (white) and at the distal end (light gray) of the bony ray consists of nanospheres of amorphous mineral. The spheres have a diameter of around 12 nm.

**Cryo-SEM Imaging.** Cryo-SEM images of frozen-hydrated newly mineralized fin bone matrix (Fig. 4*A*) and mature fin bone (Fig. 4*B*) are strikingly different. The newly formed bone mineral is dominated by spherical particles, whereas the mature bone mineral is plate-shaped. These results are consistent with the morphologies deduced from SAXS analysis. Because the particles are partially embedded within the collagen matrix, it is difficult to determine their exact sizes in the electron micrographs. The spheres appear to have diameters ranging from 10 to 20 nm. Note that Mahamid et al. (6) showed similar images, but of extracted dried specimens (see also Fig. S5).

Cryoimaging of tissue cryosectioned transverse to the fin ray long axis (Fig. 4 *C*–*E*) and cryofractured longitudinally (Fig. 4 *F*–*K*) show that the dense mineralized bone is surrounded by a nonmineralized collagenous matrix (marked M; ~2 μm thick at the bone edge in transverse direction), which is in contact with the cellular tissue. These are the growth zones leading to thickening of the ray segments. The extracellular matrix contains globular entities, 200–500 nm in diameter, which appear to be rich in calcium on the basis of the backscattered electron images (Fig. 4 *C*–*K*, *White Arrowheads*). Energy dispersive spectroscopy analyses in the SEM showed that the globules contain both calcium and phosphate, with Ca/P ratios equal to or larger than 1.3. Thus, for simplification the globules are referred to as mineralized or mineral-bearing. They are continuously dispersed from the interface with the cellular tissue to the mineralized bone matrix. Mineral bodies of similar size, termed microspheres, were previously associated with mineralizing bone (24, 25). These bodies were shown to be composed of noncrystalline subparticles.

The cellular tissue surrounding the bone contains a large number of vesicles, indicating high cellular activity (Fig. 4*D*, *Bottom*). Some of the vesicles are observed fusing into the collagen extracellular matrix (Fig. 4*C*, *Top Right*). Many of these vesicles do not produce a clear signal in the backscattered electron images. Some vesicles, however, do produce a signal in the backscattered image (Fig. 4 *F* and *G*, delineated vesicle). These mineralized vesicles are observed inside cells in longitudinal freeze fractured surfaces and contain a dense, nanogranulated material (Fig. 4*G*, *Inset*). Detailed observation of the growth zones close to the mineralized bone shows that the newly assembled, nonmineralized matrix contains mineral-bearing globules that exist as separate entities within the collagen matrix (Fig. 4 *H* and *I*, *White Arrowheads*) and fuse with the bulk mineralized bone. The fused entities form a local mineralization front that is different in texture from the adjacent more mature mineralized bone, because they appear to be composed of spheres, 10–15 nm in diameter (Fig. 4*I*, *Inset*). We also noted that the mineral-bearing globules appear to be fusing into the collagen fibrils within the growth zone (Fig. 4 *J* and *K*). All mineral particles observed inside the cell (Fig. 4 *F* and *G*), at the mineralization front (Fig. 4 *H* and *I*), or in the bulk of newly mineralized bone (Fig. 4*A*) have similar sizes and texture.

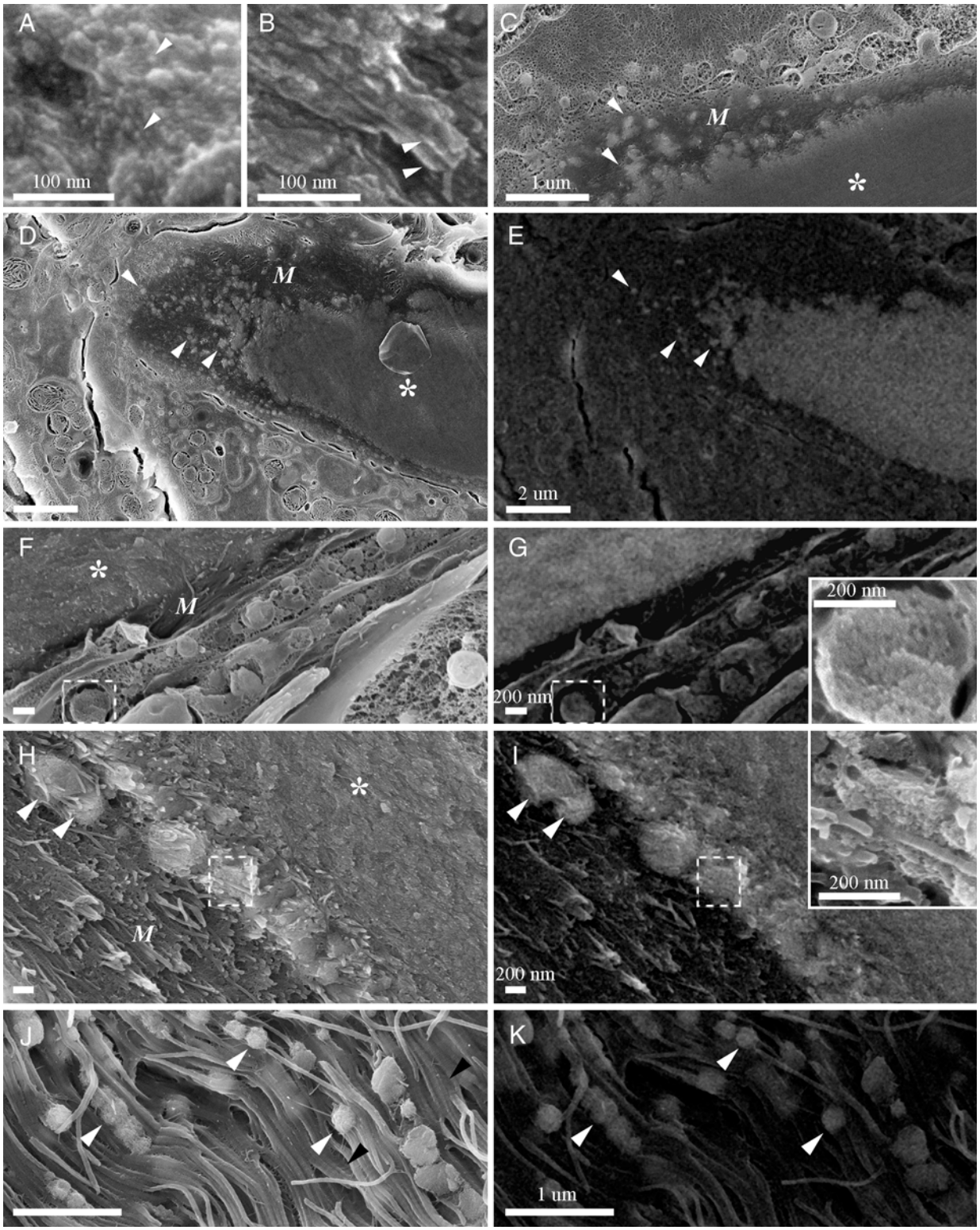


**Fig. 4.** (*A* and *B*) High-resolution cryo-SEM images of newly mineralized and mature-mineralized bone. (*A*) Distal, newly mineralized bone showing spherical mineral particles (*Arrowheads*). (*B*) Mature bone showing mineral particles in the shape of thin platelets (*Arrowheads*). (*C–K*) Cryo-SEM micrographs of the bone growth zone in high pressure frozen caudal fin tissue. (*C*, *D*, *F*, *H*, and *J*) Secondary electrons images. (*E*, *G*, *I*, and *K*) Backscattered electrons images of *D*, *F*, *H*, and *J*; asterisks—bone; M—nonmineralized matrix; white arrowheads—large globular mineralized entities. (*C–E*) Tissue cryosectioned transverse to the fin ray long axis (Fig. 1*B*: red plane). (*F–K*) Tissue freeze fractured parallel to the fin ray long axis (Fig. 1*B*: blue plane). (*Inset* in *G*) Higher magnification of delineated intracellular vesicle from *F*, which gives a backscattered electron signal in *G*. The mineral packet is nanostructured. (*H* and *I*) The newly deposited, nonmineralized bone matrix (M) contains large, mineral-bearing globular entities. The globules fuse into the mineralizing bone matrix. (*Inset* in *I*) Higher magnification of delineated area from *H*, showing the nanosphere subparticles composing the large mineral globules. (*J* and *K*) Mineral-bearing globules infusing the collagen fibrils within the growth zone. Black arrowheads—collagen banding.

## Discussion

Here we show that the growth zones of forming fin bones contain ACP, and at the continuous mineralization front the spherical ACP particles change shape and become crystalline platelets of carbonated hydroxyapatite, the mineral phase of mature bone. Because the bone segments grow continuously without undergoing remodeling, the central parts of the mature bones correspond to regions of forming bone that thickened three- or fourfold (Fig. 1*C* and Fig. S1). These core regions are composed of crystalline mineral that during formation consisted of ACP (Fig. 2). ACP is thus demonstrated to be a transient precursor phase of fish fin bone.

The evidence for the presence of ACP in the growth zone is based on the demonstration of broad WAXD peaks centered at 3.23 Å. These peaks were obtained only at the periphery of the mature bone, within a distance of 10 μm from the crystalline mineral. This distance is in agreement with the few-micrometers-thick growth zone found at the periphery of the bulk mineralized bone observed with cryo-SEM. This zone contains submicron-sized mineral-bearing globules. We note that synthetic ACP produces a broad peak in a position different from that of biogenic ACP; similar differences in short-range order between biogenic and synthetic amorphous minerals have been reported for calcium carbonates (26). The low Ca/P ratio of the mineral phase in the growth zones is also consistent with the presence of ACP (4). The biogenic ACP observed directly in the cryo-SEM and indirectly by using SAXS has a spherical morphology characteristic of amorphous minerals. Both methods show that the spheres have diameters between 10 and 20 nm. ACP nanospheres are known to form and be stabilized in vitro by bone associated proteins such as fetuin (27), osteopontin (28), and amelogenin (29).

The cryo-SEM observations show that vesicles in the cells adjacent to the bone growth zone contain mineral in relatively large bodies. In the extracellular matrix, the mineral is found as isolated submicron-sized globules in association with the collagenous matrix. These bodies are composed of nanospherical subparticles, which are presumably amorphous. Close to the continuous mineralization front, the globules merge with each other. In the mineralization front the ACP nanospheres are interspersed around the collagen fibrils, before becoming part of the crystalline mature bone. We infer that this is the zone where ACP crystallizes.

It is not unlikely that acidic macromolecules operating in parallel intracellularly and extracellularly sequester calcium and phosphate and stabilize an amorphous phase. The amorphous nanospheres may be hydrated complexes of macromolecules and inorganic mineral, forming a phase that may more easily infiltrate the collagen matrix, where the mineral particles crystallize. A similar mechanism was proposed for the in vitro liquid-precursor-directed collagen mineralization process by Olszta et al. (3). In this study anionic polypeptides are utilized to induce the formation and to stabilize an amorphous precursor phase. Interestingly, anionic nonproteinaceous polymer complexes, such as calcium polyphosphates, were found to be present at sites of new bone formation, where they are suggested to serve as bioavailable transient storage sites of calcium and phosphate. Polyphosphate complexes may also transiently stabilize an amorphous precursor phase (30).

## Conclusions

We demonstrate by using WAXD/SAXS mapping and cryo-SEM imaging that, within the native mineralizing fin bones, submicron-sized packages of ACP nanospheres are delivered from inside the cells to the preformed extracellular collagen matrix. These mineral packets then fuse into the collagen fibrils. At the mineralization front, the spherical ACP particles transform by an as yet unknown mechanism into crystalline platelets of carbonated hydroxyapatite, the mineral phase of mature bone. The use of a transient amorphous precursor appears to be an effective strategy for mineral delivery and collagen mineralization in fin bones of zebrafish. The end product of this mineralization process resembles the basic structural unit present in all vertebrate bones, including those of mammals.

## Materials and Methods

**Microbeam SAXS, WAXD, and XRF.** TL zebrafish males, 1–2 yr old, were kindly provided by Salim Seyfried from the Max-Delbrück-Center for Molecular Medicine, Berlin, Germany. Caudal fin tissues were freshly dissected before measurement, briefly washed with acetone to remove solute ions and assist dehydration, and then air dried and mounted on a flat glass capillary tip (VitroCom). In situ SAXS/WAXD and calcium XRF measurements were simultaneously obtained at the μ-Spot beamline (31), synchrotron radiation facility BESSY II, Helmholtz-Zentrum Berlin für Materialien und Energie. Samples were mounted on a *y*–*z* scanning table. Linear scans of the sample in areas of interest were performed with a step size of 10 μm. The microbeam was defined by a toroidal mirror and a pinhole of 10 μm diameter close to the sample, providing a beam size of approximately $10 \times 10$ μm$^2$ at the sample position. An energy of 13.3 keV ($\lambda = 0.9315$ Å) was selected by a Mo/BC multilayer monochromator. Fluorescence spectra were collected with an energy-sensitive detector (Ketek) in transmission geometry at an angle of about 45°. The K-shell fluorescence yield of calcium, normalized to the primary beam intensity, was used to qualitatively map the position of bone segments within the tissue. Because of the nonplanar surface of the fin samples and variations in the sample thickness, the results are not quantitative. The 2D SAXS/WAXD patterns were measured by using a MarMosaic 225 CCD-based area detector (Rayonix) placed at a sample-detector distance of 283 mm. The beam center at the detector and the sample-detector distance were calibrated by using a powder x-ray diffraction pattern of synthetic hydroxyapatite powder standard (Biorad). Typical measurement times for a single frame were 30–120 s. Radial integration of the 2D scattering patterns was performed by using Fit2D (32). The data were normalized with respect to the primary beam monitor (an ionization chamber) and corrected for background because of pinhole and air scattering. WAXD patterns were also corrected for tissue background scattering: normalization to the average intensity for $q = 9$–$14$ nm$^{-1}$, a region where only organic tissue scattering contribution was observed, and then tissue background subtraction. The signals in the WAXD were fitted with a polynomial background and then peak fitted by using Voight functions (detailed in Fig. 3 and Fig. S2). Tissue background was not subtracted for SAXS analysis, because the contribution of the organic tissue, which varied in thickness, could not be quantified for the small-angle region. Differences in the shape of SAXS profiles were evaluated qualitatively. Specifically, we compared the experimental data with the calculated scattering function of spheres: $I(q, r) \propto ((\sin(qR) - qr(\cos(qR))/(qr)^3)^2$, where $r$ is the radius of the sphere (23). Mineral platelet thickness evaluation was performed for typical bone scattering profiles as previously reported (21).

**Cryo-SEM.** Fragments of about $2 \times 2$ mm$^2$ were cut from freshly dissected caudal fins of TL zebrafish provided by Gil Levkowitz, Weizmann Institute of Science. The samples were immediately immersed in 10% dextran (Fluka), sandwiched between two metal discs (3 mm diameter, 0.1-mm cavities) and cryoimmobilized in a high-pressure freezing device (HPM10; Bal-Tec). The frozen samples were mounted on a holder under liquid nitrogen and transferred to a freeze fracture device (BAF 60; Bal-Tec) by using a vacuum cryotransfer device (VCT 100; Bal-Tec). Samples were fractured at a temperature of −140 °C, etched for 20 min at −105 °C at a vacuum better than $5 \times 10^{-7}$ mbar, and coated with 2.5 nm Pt/C by double axis rotary shadowing. This preparation was used to generate a longitudinal view of the bones (Fig. 1*B*, *Blue Plane* and Fig. 4 *F*–*K*). Alternatively, frozen samples were transferred to a cryoultramicrotome (Leica) and cryosectioned by using a 20° trimming diamond knife (Diatome) for the production of transverse view of the bones (Fig. 1*B*, *Red Plane* and Fig. 4 *C*–*E*) (33). These samples were then transferred to the BAF 60 for etching and coating as described above. Samples were observed in an Ultra 55 SEM (Zeiss) by using a secondary electron in-lens detector and a backscattered electron in-lens detector (operating at 5 kV) in the frozen-hydrated state by use of a cryostage at a temperature of −120 °C. Some samples were freeze dried after observation in the BAF 60, brought to room temperature, transferred to a Supra SEM (Zeiss), and analyzed by energy dispersive spectroscopy. Image brightness and contrast levels and median filtering (2–4 pixels) of backscattered electrons images were adjusted by using Adobe Photoshop.

High-resolution microcomputed tomography images generated from x-ray radiographs (GE Healthcare) were obtained from air-dried fresh TL caudal fins as previously reported (6).

**ACKNOWLEDGMENTS.** We thank Dr. Salim Seyfried and Dr. Gil Levkowitz for providing the animals and Dr. Amnon Sharir for the μ-CT measurements. We thank Christoph Gilow and Dr. Ivo Zizak for help during the synchrotron experiments and Ingrid Zenke for laboratory WAXD measurements. The x-ray studies were conducted at the μ-Spot beamline of the BESSY II synchrotron radiation facility, which is part of the Helmholtz-Zentrum Berlin für Materialien und Energie, and were partially supported by the European Integrated Infrastructure Initiative I3 in FP6. The electron microscopy studies were conducted at the Irving and Cherna Moskowitz Center for Nano and Bio-Nano Imaging, Weizmann Institute of Science. L.A. is the incumbent of the Dorothy and Patrick Gorman Professorial Chair of Biological Ultrastructure, and S.W. is the incumbent of the Dr. Trude Burchardt Professorial Chair of Structural Biology. J.M. was supported by the Israeli Council for Higher Education. This research was supported in part by the Israel Science Foundation.

1. Weiner S (2006) Transient precursor strategy in mineral formation of bone. *Bone* 39:431–433.
2. Grynpas MD, Omelon S (2007) Transient precursor strategy or very small biological apatite crystals?. *Bone* 41:162–164.
3. Olszta MJ, et al. (2007) Bone structure and formation: A new perspective. *Mat Sci Eng R* 58:77–116.
4. Christoffersen J, Christoffersen MR, Kibalczyc W, Andersen FA (1989) A contribution to the understanding of the formation of calcium phosphates. *J Cryst Growth* 94:767–777.
5. Crane NJ, et al. (2006) Raman spectroscopic evidence for octacalcium phosphate and other transient mineral species deposited during intramembranous mineralization. *Bone* 39:434–442.
6. Mahamid J, Sharir A, Addadi L, Weiner S (2008) Amorphous calcium phosphate is a major component of the forming fin bones of zebrafish: Indications for an amorphous precursor phase. *Proc Natl Acad Sci USA* 105:12748–12753.
7. Beniash E, Metzler RA, Lam RS, Gilbert PU (2009) Transient amorphous calcium phosphate in forming enamel. *J Struct Biol* 166:133–143.
8. Deshpande AS, Beniash E (2008) Bio-inspired synthesis of mineralized collagen fibrils. *Cryst Growth Des* 8:3084–3090.
9. Weiner S, et al. (2009) Overview of the amorphous precursor phase strategy in biomineralization. *Front Mater Sci China* 3:104–108.
10. Paris O (2008) From diffraction to imaging: New avenues in studying hierarchical biological tissues with x-ray microbeams (review). *Biointerphases* 3:Fb16–Fb26.
11. Burger C, et al. (2008) Lateral packing of mineral crystals in bone collagen fibrils. *Biophys J* 95:1985–1992.
12. Chen J, et al. (2005) *In vitro* mineralization of collagen in demineralized fish bone. *Macromol Chem Physic* 206:43–51.
13. Ge J, Cui FZ, Wang XM, Wang Y (2007) New evidence of surface mineralization of collagen fibrils in wild type zebrafish skeleton by AFM and TEM. *Mat Sci Eng C-Bio S* 27:46–50.
14. Ge J, Wang XM, Cui FZ (2006) Microstructural characteristics and nanomechanical properties across the thickness of the wild-type zebrafish skeletal bone. *Mat Sci Eng C-Bio S* 26:710–715.
15. Landis WJ, Geraudie J (1990) Organization and development of the mineral phase during early ontogenesis of the bony fin rays of the trout *Oncorhynchus mykiss. Anat Rec* 228:383–391.
16. Becerra J, Montes GS, Bexiga SR, Junqueira LC (1983) Structure of the tail fin in teleosts. *Cell Tissue Res* 230:127–137.
17. Montes GS, et al. (1982) Fine structure and histochemistry of the tail fin ray in teleosts. *Histochemistry* 75:363–376.
18. Ferreira L, Beamish R, Youson J (1999) Macroscopic structure of the fin-rays and their annuli in pectoral and pelvic fins of chinook salmon, *Oncorhynchus tshawytscha. J Morphol* 239:297–320.
19. Frenkel V, Kindschib G, Zohar Y (2002) Noninvasive, mass marking of fish by immersion in calcein: Evaluation of fish size and ultrasound exposure on mark endurance. *Aquaculture* 214:169–183.
20. Fratzl P, et al. (2005) Diffracting "stacks of cards"—Some thoughts about small-angle scattering from bone. *Prog Coll Pol Sci S* 130:33–39.
21. Fratzl P, et al. (1991) Nucleation and growth of mineral crystals in bone studied by small-angle x-ray-scattering. *Calcif Tissue Int* 48:407–413.
22. Fratzl P, Schreiber S, Klaushofer K (1996) Bone mineralization as studied by small-angle x-ray scattering. *Connect Tissue Res* 35:9–16.
23. Guinier A, Fournet G (1955) *Small-Angle Scattering of X-Rays* (Wiley, New York).
24. Gay C, Schraer H (1975) Frozen thin-sections of rapidly forming bone: Bone cell ultrastructure. *Calcif Tissue Res* 19:39–49.
25. Carter DH, Hatton PV, Aaron JE (1997) The ultrastructure of slam-frozen bone mineral. *Histochem J* 29:783–793.
26. Addadi L, Raz S, Weiner S (2003) Taking advantage of disorder: Amorphous calcium carbonate and its roles in biomineralization. *Adv Mater* 15:959–970.
27. Heiss A, et al. (2003) Structural basis of calcification inhibition by alpha 2-HS glycoprotein/fetuin-A. Formation of colloidal calciprotein particles. *J Biol Chem* 278:13333–13341.
28. Holt C, Sorensen ES, Clegg RA (2009) Role of calcium phosphate nanoclusters in the control of calcification. *FEBS J* 276:2308–2323.
29. Kwak SY, et al. (2009) Role of 20-kDa amelogenin (P148) phosphorylation in calcium phosphate formation in vitro. *J Biol Chem* 284:18972–18979.
30. Omelon S, et al. (2009) Control of vertebrate skeletal mineralization by polyphosphates. *PLoS One* 4:e5634.
31. Paris O, et al. (2007) A new experimental station for simultaneous x-ray microbeam scanning for small- and wide-angle scattering and fluorescence at BESSY II. *J Appl Crystallogr* 40:S466–S470.
32. Hammersley AP (1997) *FIT2D: An Introduction and Overview* (European Synchrotron Radiation Facility, Grenoble) internal report.
33. Richter T, et al. (2007) Pros and cons: Cryo-electron microscopic evaluation of block faces versus cryo-sections from frozen-hydrated skin specimens prepared by different techniques. *J Microsc* 225:201–207.